Accretion History of AGN: Multiwavelength Comparison of X-ray and Infrared Selected Active Galactic Nuclei

Thresa Kelly[a,b], Connor Auge[a], David Sanders[a]

[a]*Institute for Astronomy, University of Hawai'i, 2680 Woodlawn Drive, Honolulu, HI 96822, USA*
[b]*Department of Physics & Astronomy, University of Kansas, Lawrence, KS 66045, USA*

Abstract

Active galactic nuclei (AGN) have different emission spectra depending on their physical characteristics. Using only one wavelength region to identify an AGN may miss sources with unique characteristics. In this work, we compare the multiwavelength properties of X-ray and mid-IR selected AGN in the COSMOS field. Our X-ray sample includes all sources with a $0.5-10$ keV X-ray luminosity greater than 10^{43} erg s^{-1}. We define our mid-IR AGN sample using the four *Spitzer*/IRAC channels. We find that 65% of X-ray selected AGN are not identified as AGN using their IR colors, and 47% of IR-selected AGN do not meet the X-ray luminosity threshold. We find that IR selected AGN are more luminous in the MIR than X-ray selected AGN, but have a similar range of UV emissions. Sources that satisfy both IR and X-ray selection criteria are more luminous across their entire spectra, in general.

1. Introduction

Active galactic nuclei (AGN) are luminous sources in the centers of galaxies that are powered by matter accretion onto a supermassive black hole (SMBH). The unified model for AGN includes the central SMBH, accretion disk, dusty torus, and relativistic jets (Urry & Padovani, 1995). The different physical features produce characteristic emission in different wavelength regimes: the non-thermal emission and jets produce gamma-rays and radio waves, the SMBH corona emits in the X-ray, the accretion disk produces ultraviolet (UV) light, and the obscuring gas and dust emits in the infrared (IR) (Padovani et al., 2017). AGN have detectable emissions across the entire electromagnetic spectrum, and can be discovered in all spectral bands. This work focuses on X-ray and IR emissions.

The accretion disk produces a large number of photons, which are processed into X-rays through inverse Compton scattering in the corona (Hickox & Alexander, 2018). The X-ray photons interact with the accretion disk and obscuring dust by scattering, reflection, and photo-electric absorption (Padovani et al., 2017). Some types of AGN are heavily obscured by a dusty torus which absorbs the emission from the accretion disk and reprocess the energy in to the IR region (Padovani et al., 2017).

The observed spectral properties of the AGN depends on the line-of-sight viewing angle (Urry & Padovani, 1995). The X-ray and UV observations are most luminous when the inclination approaches the AGN-s rotation axis. Observed X-ray emission is least luminous when the line-of-sight is directed through the AGN's dusty torus. In contrast, the IR observations are brightest for heavily obscured AGN when the viewing angle is through the torus and dimmest when the line-of-sight is inclined toward the rotation axis (Elvis et al., 1994; Richards et al., 2004).

X-ray observations are highly effective in selecting AGN. Most galactic processes have X-ray luminosities less than 10^{43} erg s^{-1}, so an X-ray selected AGN sample has very little contamination (Ranalli et al., 2003). However, an X-ray selection may miss heavily obscured AGN (Assef et al., 2015). A dusty torus with a column density greater than 3×10^{23} cm^{-2} can significantly obscure the AGN X-ray emission (Padovani et al., 2017). These affects are more prominent for large redshifts, as increasing redshift increases the rest frame energies. The absence of heavily obscured AGN in an X-ray selected AGN sample can induce bias. So, it is important to consider other AGN selection methods.

Mid-infrared (MIR) AGN selection is particularly successful in identifying obscured sources; IR wavelengths are less sensitive to neutral hydrogen absorption than X-rays (Padovani et al., 2017). However, MIR selections can be contaminated by non-AGN sources: strongly star forming galaxies, z & 1 galaxies, brown dwarf stars, and young stellar objects (Assef et al., 2013; Hickox & Alexander, 2018). AGN without a dense dusty torus may be missed in a MIR selected AGN sample, which can induce bias when trying to make conclusions about AGN and galaxies in general.

In this work, we compare the multiwavelength properties of AGN independently identified by X-ray and MIR selection methods. We describe the data catalogs and AGN selection methods in §2. We show our results from the X-ray and MIR comparison and spectral energy distributions in §3. Lastly, §4 presents our conclusions and future work. We assume a standard cosmology with $H_0 = 70$km s^{-1} Mpc^{-1}, $\Omega_m = 0.3$, and $\Omega_\Lambda = 0.7$.

2. Method

2.1. Data Catalogs

This work utilizes data from the Cosmic Evolution Survey (COSMOS) survey. It is a deep multiwavelength survey over an area of 2 deg^2. It is centered on +150.119 right ascension and +2.205 declination at J2000. This field has photometric measurements ranging from the X-ray to radio wavelengths (Scoville et al., 2007).

The *Chandra* COSMOS-Legacy Survey (C-COSMOS) contains X-ray photometry for 4016 sources with their optical/IR counterparts. This survey covers 2.2 deg^2 of the COSMOS field (Marchesi et al., 2016). We use these measurements to identify AGN, as shown in §2.2.

The COSMOS2020 data release contains multiwavelength photometry for 1.7 million sources (Weaver et al., 2022). The catalog includes data from the Galaxy Evolution Explorer (GALEX), Canada–France–Hawaii telescope (CFHT), Hubble Space Telescope (HST), Subaru, Ul-

traVISTA, and *Spitzer* telescopes. The instruments cover the UV, optical, and IR wavelength regimes (Weaver et al., 2022). We use the *Spitzer*/IRAC channels when identifying our IR-selected sample, which is described in §2.3. We also use the multi-wavelength photometry to create spectral energy distributions (SED) for our AGN sources, as described in §3.3.

Both COSMOS catalogs have photometric and spectroscopic redshifts. We use spectroscopic redshifts when possible and photometric redshifts if no spectroscopic redshift is available.

2.2. X-ray AGN Selection

X-ray observations are a useful tool for identifying AGN. Nearly all AGN emit in the X-ray band, with the most luminous reaching X-ray luminosities (L_x) up to 10^{46} erg s^{-1} (Ranalli et al., 2003).

The most significant contaminant when selection AGN using X-ray luminosity (L_x) are X-ray luminous binary star systems. These occur when a degenerate star accretes matter from its companion. This emission can be $L_X \approx 3 \times 10^{42}$ erg s^{-1} in star forming regions with formation rates about 1000 M$_\odot$ yr^{-1} (e.g. Lehmer et al. 2010; Mineo, Gilfanov, & Sunyaev 2012a). Another contaminant are thermal X-ray emissions from hot gas. These sources can reach $L_X \approx 10^{45}$ erg s^{-1} in the cores of massive galaxies (e.g. Stanek et al. 2006; Ebeling et al. 2010).

In this work, we identify sources with intrinsic $0.5 - 10$ keV X-ray luminosities greater than 10^{43} erg s^{-1} as AGN. This yields a reliable selection of AGN.

We use the C-COSMOS to acquire our X-ray selected AGN sample. We exclude any sources without a valid redshift or a multiwavelength counterpart in Laigle et al. (2016), which leaves us with 2648 sources. This sample is shown in Figure 1. We identify 2232 AGN that satisfy our 10^{43} erg s^{-1} X-ray luminosity requirement. To be consistent with out MIR selected sample (see §2.3), we exclude any sources without COSMOS2020 photometric measurements in the four *Spitzer*/IRAC channels. To ensure good MIR data quality, we require that all sources have a 24 μm detection with a fractional error less than 50%. This leaves us with 1517 sources in our final X-ray selected AGN sample.

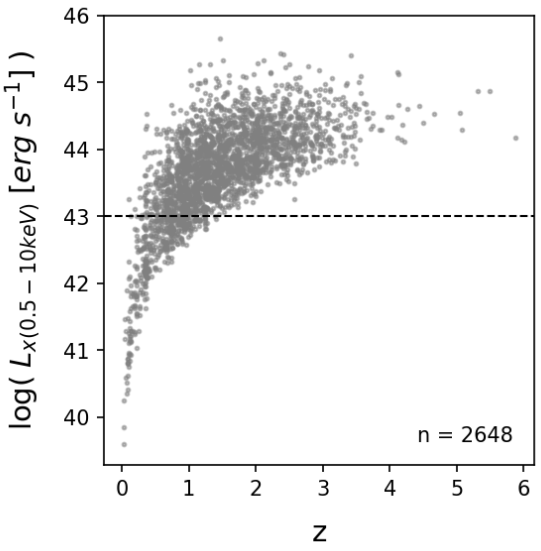

Figure 1: The rest frame $0.5 - 10$ keV X-ray luminosity versus redshift. Out of the 2648 sources, there are 2232 sources above the dotted line at 10^{43} erg s^{-1}.

2.3. Infrared AGN Selection

IR observations are useful for identifying dust obscured AGN, as the dusty torus of an AGN emits in the IR between 5 μm and 30 μm (Sanders et al., 1988).

There are different contaminating sources for far, near, and mid-infrared regions. Dust emission in star-forming galaxies can have similar luminosities to obscured AGN, but are often cooler in temperature ($\leq$ 40 K) and dominate in the far-infrared (FIR) (Magnelli et al., 2012). The stellar peak at 1.6 μm can make it difficult to identify AGN in near-infrared (NIR) wavelengths Padovani et al. (2017). There are a variety of contaminants in the MIR region that can mimic AGN: (1) Brown dwarfs for $z > 5$ (Stern et al., 2007); (2) Young stellar objects (Koenig et al., 2012); (3) Star forming galaxies with strong polycyclic aromatic hydrocarbon emission at $z \sim 0.2$ (Padovani et al., 2017); and (4) massive galaxies at z & 1 where the 1.6 μm stellar bump is redshifted into the MIR.

The MIR selection method from Donley et al. (2012) was designed to avoid redshifted galaxies, which are the most significant contaminant in deep surveys like COSMOS. This method has a high reliability and completeness when compared to other selections (Assef et al., 2013). The AGN selection criteria makes use of the four *Spitzer*/IRAC channels: 3.6, 4.5, 5.8, and 8.0 μm. Any sources that fall within the wedge defined by

$$\begin{aligned} x &= \log(f_{5.8}/f_{3.6}), \\ y &= \log(f_{8.0}/f_{4.5}) \end{aligned} \tag{1}$$

$$\begin{aligned} &(x \geq 0.08) \ \wedge \ (y \geq 0.15) \wedge \\ &(y \geq 1.21x - 0.27) \wedge \\ &(y \leq 1.21x + 0.27) \wedge \\ &(f_{4.5} > f_{3.6}) \ \wedge \ (f_{5.8} > f_{4.5}) \wedge \\ &(f_{8.0} > f_{5.8}) \end{aligned} \tag{2}$$

are AGN ($\wedge$ means "and") (Donley et al., 2012).

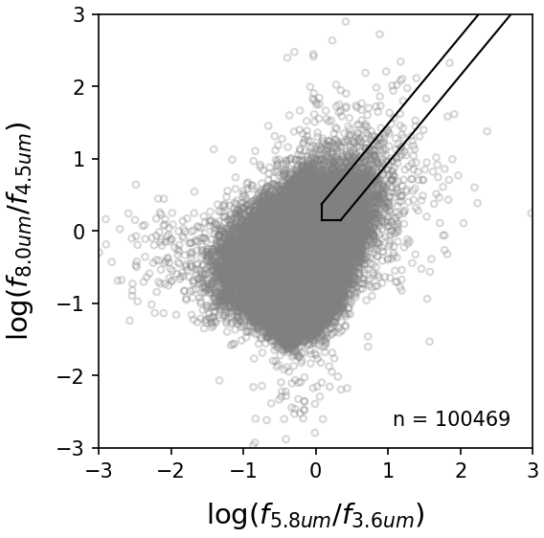

Figure 2: *Spitzer*/IRAC infrared color-color plot for 100469 sources. There are 1533 AGN within the Donley et al. (2012) wedge.

For our MIR AGN sample, we use sources from COSMOS2020 that have redshifts and a corresponding detection in Laigle et al. (2016). We plot all sources with detections in all four *Spitzer*/IRAC channels in Figure 2. We identify 1533 AGN using the Donley et al. (2012) criteria. We then reduce our sample to include only those that have a 24 μm detection with a fractional error less than 50%. Our final MIR selected AGN sample includes 1009 sources.

3. Results and Discussion

3.1. X-ray Luminosity

There are 1993 total AGN selected by the X-ray and MIR criteria. About 77% of our sample have an X-ray detection in C-COSMOS. This is made of the 1517 X-ray selected AGN along with 15 MIR selected AGN with $L_X < 10^{43}$ erg s^{-1}. We utilize

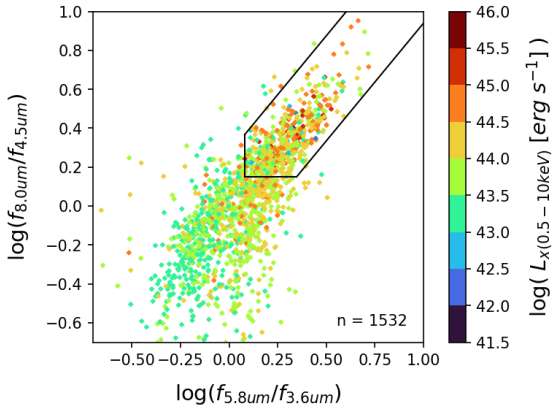

Figure 3: *Spitzer*/IRAC IR color-color plot for 1532 AGN with 0.5 – 10 keV X-ray luminosity on the colorbar. The black wedge illustrates the Donley et al. (2012) AGN selection criteria.

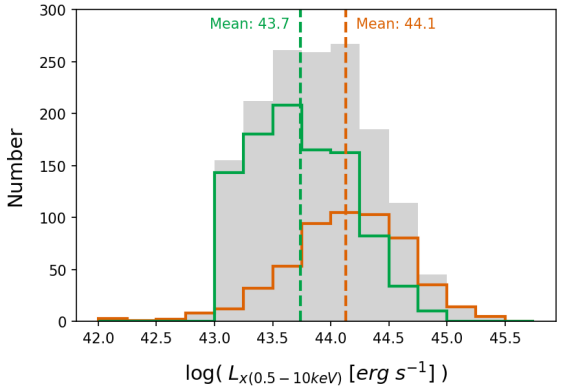

Figure 4: Histogram of the 0.5 – 10 keV X-ray luminosities for the AGN in Figure 3. The green line represents the 984 AGN outside the Donley et al. (2012) wedge. The orange line shows the 548 AGN inside the wedge. The gray bars show the sum total 1532 AGN. The sources inside the wedge have higher luminosities on average.

any source with an X-ray detection to analyze the X-ray luminosities as a function of MIR color.

Figure 3 shows the X-ray luminosity distribution with respect to the Donley et al. (2012) wedge. In general, the less X-ray luminous AGN have the smallest MIR color fractions. The most luminous sources have the greater MIR colors. The luminosity tends to increase along the power law.

We plot the histograms of sources inside and outside the Donley et al. (2012) wedge in Figure 4. 36% is inside the wedge and 64% of the sample is outside the wedge. The mean X-ray luminosity inside the wedge is 2.5 times greater than the mean outside the wedge. The luminosities within the wedge have a wider distribution, reaching the lowest and highest X-ray luminosities. It is expected that the sources outside the wedge have a greater minimum luminosity as they are required to have $L_x > 10^{43}$ erg s^{-1}; those inside the wedge are unrestricted.

The intrinsic X-ray luminosity from an AGN is correlated to the power. More activity in the AGN increases the energy output. As the most X-ray luminous sources have bright MIR colors, the Donley et al. (2012) selecting wedge is most adept at identifying the most powerful AGN. Weaker AGN are missed by this selection method.

3.2. Selection Method

We split our 1517 X-ray selected and 1009 MIR selected AGN sample into three groups: exclusive X-ray, exclusive MIR, and inclusive X-ray and MIR. The exclusive X-ray group includes sources that have $L_{x(0.5-10keV)} > 10^{43}$ erg s^{-1} but do not satisfy the MIR selection criteria. The exclusive MIR group includes sources who fall inside the Donley et al. (2012) wedge but have no X-ray detections or detections less than 10^{43} erg s^{-1}. The inclusive X-ray and MIR group includes sources that meet both the X-ray and MIR selection requirements. The number of sources in each selection group

AGN selection method	Figure color key	Number of AGN	
		$z < 6$	$z \leq 1$
Exclusive X-ray	Blue	984	276
Exclusive IR	Red	476	93
Inclusive X-ray and IR	Yellow	533	86
Sum total of AGN		1993	455

Table 1: Number of AGN by selection method and redshift range. For all redshifts, there are 1517 AGN in the full X-ray sample 1009 AGN in the full IR sample; 533 AGN are identi ed by both selection methods. The numbers in this table match the sources in Figure 5.

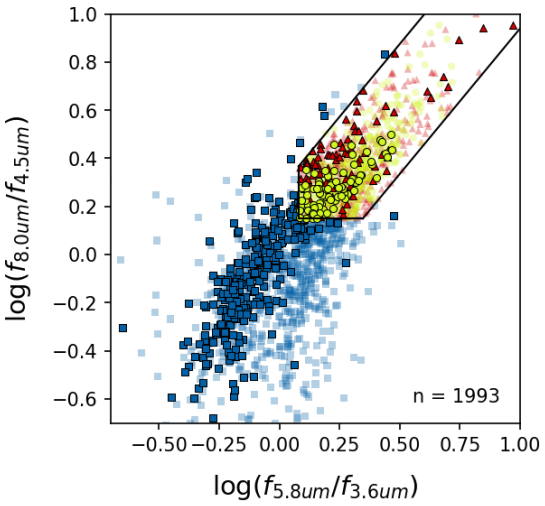

Figure 5: *Spitzer*/IRAC IR color-color plot for different AGN selection methods. The black lines make up the Donley et al. (2012) AGN selection wedge. The blue squares are X-ray exclusive AGN, the red triangles are MIR exclusive AGN, and the yellow circles are X-ray and MIR inclusive AGN. The solid points with black edges have redshifts less than 1.

and redshift range is shown in Table 1. The placement of these same sources in MIR color space are shown in Figure 5.

From our total 1993 AGN sample, 65% of X-ray selected AGN are not identified by the Donley et al. (2012) selection criteria. 47% of MIR selected AGN do not have X-ray luminosities greater than 10^{43} erg s^{-1}. There is limited overlap between the two selection methods, so neither sample captures all types of AGN.

In order to analyze the multiwavelength properties (beginning in §3.3), we make a subsample of sources with $z \leq 1$. We need low redshift sources when analysing MIR rest frame emission. The MIR data gets shifted into the near-IR and optical wavelengths at higher redshifts, so analysis becomes considerably more difficult.

For our 455 AGN sample with $z \leq 1$, 76% of X-ray selected AGN fall outside the wedge and 52% of IR selected AGN are not X-ray luminous. For low redshifts, the X-ray selection method captures a significant fraction of the total AGN sample.

3.3. Spectral Energy Distributions

We create spectral energy distributions (SEDs) for our 455 $z \leq 1$ AGN sources. We use photometry from the COSMOS2020 catalog; the GALEX, Subaru, VISTA, *Spitzer*, and Herschel telescopes cover the the far-ultraviolet to far-infrared wavelengths. Details about the telescopes, filters, and reference wavelengths are given in Table A.1 in the Appendix.

To make the SEDs, we convert the energy flux (F_ν) into photon flux (F_λ). Then we normalize the SED for each source by divid-

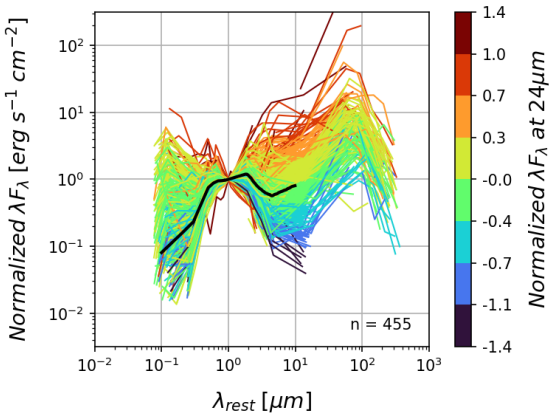

Figure 6: SEDs for 455 AGN with $z \leq 1$ normalized at 1 μm. The axis shows, in log scale, the energy density versus rest wavelength. The color bar shows the normalized energy density at observed 24 μm. The black line is the median curve.

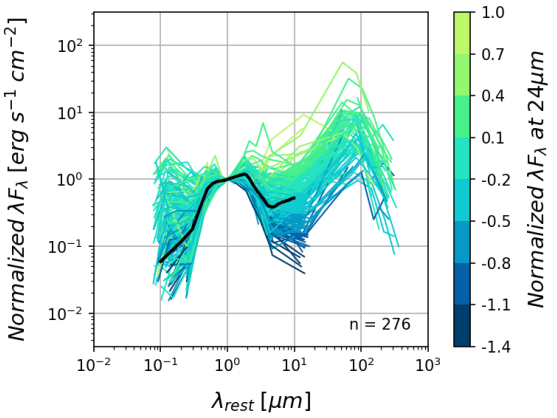

Figure 7: SED for exclusive X-ray selected AGN with $z \leq 1$ normalized at 1 μm. The colorbar shows the logarithmic normalized energy density at observed 24 μm. The black curve is the median SED for all 276 sources.

ing the curve by the interpolated value at 1 μm. We draw a median line between 0.1 μm and 10 μm. We do not plot the median above 10 μm because many of the sources do not detections in the FIR; the median line would not represent the full sample.

The SEDs for the $z \leq 1$ AGN sample is shown in Figure 6. The energy density ranges from approximately $0.01-10$ erg s^{-1} cm^{-2} in the UV ($\sim 0.15\mu$m) and $0.05-11$ erg s^{-1} cm^{-2} in the MIR ($\sim 5\mu$m). The median SED curve begins at about 0.08 erg s^{-1} cm^{-2} at 0.01 μm, then sharply increases through the UV, slightly increases through 1 μm, then decreases until 5 μm, then increases toward the FIR.

3.4. Exclusive X-ray selected AGN

We plot the SEDs for all $z \leq 1$ exclusive X-ray selected AGN in Figure 7. This includes all 276 sources that have an intrinsic $0.5-10$ keV X-ray luminosity greater than 10^{43} erg s^{-1} but fall outside the Donley et al. (2012) wedge.

The normalized energy density ranges from $0.02-2$ erg s^{-1} cm^{-2} in the UV and $0.08-8$ erg s^{-1} cm^{-2} in the MIR. This is similar to the UV energy range in the total $z \leq 1$ sample. The median SED curve begins at 0.06 erg s^{-1} cm^{-2} at 0.01 μm, then sharply increases through the UV, flattens near 1 μm, then decreases until 5 μm, and then slightly increases; this shape is very similar to the total sample, but is slightly decreased MIR.

3.5. Exclusive IR selected AGN

The SED $z \leq 1$ exclusive MIR selected AGN are shown in Figure 8. This 93 source sample includes any AGN that falls inside the Donley et al. (2012) wedge but do not have X-ray luminosities greater than 10^{43} erg s^{-1}.

The energy density ranges from $0.05-5$ erg s^{-1} in the UV and $0.9-11$ erg s^{-1} cm^{-2} in the MIR. This is a narrower range than the full $z \leq 1$ sample, especially in the MIR. The median SED curve begins at 0.1

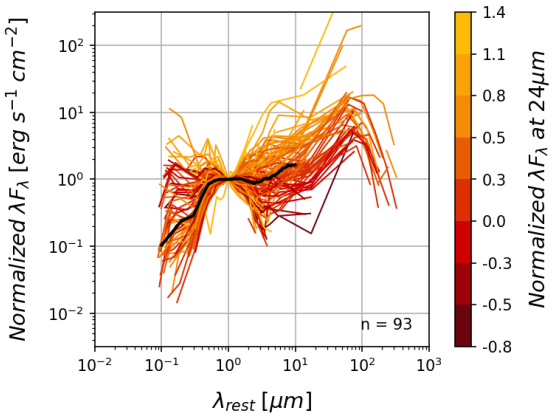

Figure 8: SED for exclusive IR-selected AGN with $z \leq 1$ normalized at $1\mu m$. The colorbar shows the logarithmic normalized energy density at observed $24\mu m$. The black curve is the median SED for all 93 sources.

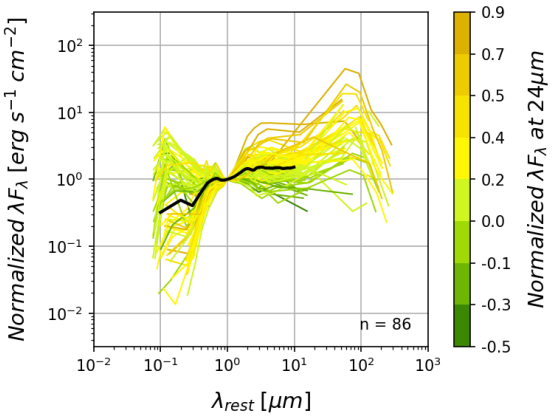

Figure 9: SED for inclusive X-ray and MIR selected AGN for $z \leq 1$. All curves are normalized at 1 μm. The colorbar shows the logarithmic normalized energy density at observed $24\mu m$. The black curve is the median SED for all 93 sources.

erg s^{-1} cm^{-2} at 0.01 μm, then generally increases through the UV, flattens near 1 μm, then decreases slightly until 5 μm, and then slightly increases. The shape of the median is different than the total sample, as it is more luminous across the MIR region.

The exclusive MIR AGN are likely very powerful AGN. Because of the X-ray luminosity distribution shown in Figure 4, this AGN sample may have very high intrinsic X-ray luminosities ($L_z > 10^{44}$ erg s^{-1}). Most of these sources do not have X-ray detections. So, the exclusive MIR sample is composed of Compton thick AGN.

3.6. Inclusive X-ray and IR selected AGN

Figure 9 shows the SEDs for the $z \leq 1$ inclusive X-ray and MIR selected AGN. These are 86 sources that meet both the X-ray and MIR requirements: they have $L_x > 10^{43}$ erg s^{-1} and fall inside the Donley et al. (2012) wedge.

The energy density ranges from $0.02 - 3$ erg s^{-1} cm^{-2} in the UV and and $0.7 - 7$ erg s^{-1} cm^{-2} in the MIR. This is the narrowest range for all AGN selection groups for both UV and MIR wavelengths. The median SED curve begins at 0.3 erg s^{-1} cm^{-2} at 0.01 μm, then jaggedly increases through the UV, slightly increases through 1 μm until $5\mu m$, and then flattens. The median is more intense in the UV and near-IR compared to both the exclusive X-ray and exclusive MIR groups.

4. Conclusions

The goal of this work is to compare the multiwavelength properties of X-ray and MIR selected AGN in the COSMOS field. We identify 1517 AGN with intrinsic $0.5 - 10$ keV X-ray luminosity greater than 10^{43} erg s^{-1} and 1009 AGN that fall inside the Donley et al. (2012) selection wedge; there are 533 AGN that are identified by both selection methods. We require that all sources in our analysis have a photometric or spectro-

scopic redshift, a multiwavelength counterpart in Laigle et al. (2016), photometric detections at 3.6, 4.5, 5.8, 8.0, and 24 μm. We use the C-COSMOS and COSMOS2020 catalogs Marchesi et al. (2016); Weaver et al. (2022).

We plot the *Spitzer*/IRAC MIR color versus color to analyze the X-ray distribution of our sample against their MIR colors. We also plot spectral energy distributions (SEDs) for the exclusive X-ray (AGN that have $L_x > 10^{43}$ erg s^{-1} but fall outside the MIR wedge), exclusive MIR (AGN that are inside the (Donley et al., 2012) selection wedge but do now meet the X-ray requirement), and inclusive X-ray and MIR (AGN that meet both the X-ray and MIR criteria) groups for $z \leq 1$.

Our primary results are as follow:

1. 77% of all 1993 AGN have an X-ray detection in C-COSMOS. Out of these sources, the most X-ray luminous AGN are identified by the Donley et al. (2012) wedge. The average X-ray luminosity is 2.5 times greater for AGN inside the wedge than those outside.
2. Neither X-ray nor MIR selection method captures the full AGN sample: 65% of all X-ray selected AGN are not identified by the (Donley et al., 2012) MIR selection criteria, and 47% of MIR selected AGN do not have X-ray luminosities greater than 10^{43} erg s^{-1}. For $z \leq 1$ these percents become 76% and 52% respectively. The X-ray method is more effective at capturing AGN for lower redshifts.
3. The SEDs for the exclusive X-ray, exclusive MIR, and inclusive all have differentiable ranges and median shapes. Sources that meet the Donley et al. (2012) requirement are overall more luminous in the MIR. The three AGN groups have a similar range of UV emission, but the exclusive X-ray AGN have the lowest average. X-ray selected AGN capture the full range of emission properties but miss Compton thick AGN that are identified by MIR colors.

When studying black hole growth or AGN-galaxy co-evolution, it is important to have a complete and uncontaminated sample of both obscured and obscured AGN. Using only one AGN selection method will significantly bias the sample. It is important to use multiple selection methods when possible.

For future research, we will be performing a more quantitative analysis of the different SED shapes present in each AGN selection group. This will allow us to form more detailed conclusions about the different types of AGN identified using each selection method. For additional future work, we will be performing a repeat analysis for surveys at other optical depths – such as Stripe82X and CDF-N/S.

Acknowledgements

Thresa Kelly acknowledges support from Research Experience for Undergraduate program at the Institute for Astronomy, University of Hawaii-Manoa funded through NSF grant #2050710.

Thresa Kelly would like to thank the Institute for Astronomy for their hospitality during the course of this project.

Some of the data presented herein were obtained at the W. M. Keck Observatory, which is operated as a scientific partnership

among the California Institute of Technology, the University of California and the National Aeronautics and Space Administration. The Observatory was made possible by the generous financial support of the W. M. Keck Foundation. This research is based [in part] on data collected at Subaru Telescope,which is operated by the National Astronomical Observatory of Japan. We are honored and grateful for the opportunity of observing the Universe from Maunakea, which has the cultural, historical and natural significance in Hawai`i. The authors wish to recognize and acknowledge the very significant cultural role and reverence that the summit of Maunakea has always had within the indigenous Hawaiian community. We are most fortunate to have the opportunity to conduct observations from this mountain.

This research made use of NumPy (Harris et al., 2020), Matplotlib (Hunter, 2007), and Astropy (Astropy Collaboration et al., 2013, 2018) Python packages.

References

Assef, R. J., Stern, D., Kochanek, C. S., et al. 2013, ApJ, 772, 26

Assef, R. J., Eisenhardt, P. R. M., Stern, D., et al. 2015, ApJ, 804, 27

Astropy Collaboration, Robitaille, T. P., Tollerud, E. J., et al. 2013, A&A, 558, A33

Astropy Collaboration, Price-Whelan, A. M., Sipőcz, B. M., et al. 2018, AJ, 156, 123

Donley, J. L., Koekemoer, A. M., Brusa, M., et al. 2012, The Astrophysical Journal, 748, 142, aDS Bibcode: 2012ApJ...748..142D. https://ui.adsabs.harvard.edu/abs/2012ApJ...748..142D

Elvis, M., Wilkes, B. J., McDowell, J. C., et al. 1994, ApJS, 95, 1

Harris, C. R., Millman, K. J., van der Walt, S. J., et al. 2020, Nature, 585, 357. https://doi.org/10.1038/s41586-020-2649-2

Hickox, R. C., & Alexander, D. M. 2018, Annual Review of Astronomy and Astrophysics, 56, 625. https://ui.adsabs.harvard.edu/abs/2018ARA&A..56..625H/abstract

Hunter, J. D. 2007, Computing in Science & Engineering, 9, 90

Laigle, C., McCracken, H. J., Ilbert, O., et al. 2016, ApJS, 224, 24

Marchesi, S., Civano, F., Elvis, M., et al. 2016, The Astrophysical Journal, 817, 34, aDS Bibcode: 2016ApJ...817...34M. https://ui.adsabs.harvard.edu/abs/2016ApJ...817...34M

Padovani, P., Alexander, D. M., Assef, R. J., et al. 2017, Astronomy and Astrophysics Review, 25, 2. https://ui.adsabs.harvard.edu/abs/2017A&ARv..25....2P/abstract

Ranalli, P., Comastri, A., & Setti, G. 2003, A&A, 399, 39

Richards, G. T., Nichol, R. C., Gray, A. G., et al. 2004, ApJS, 155, 257

Sanders, D. B., Soifer, B. T., Elias, J. H., Neugebauer, G., & Matthews, K. 1988, ApJ, 328, L35

Scoville, N., Aussel, H., Brusa, M., et al. 2007, ApJS, 172, 1

Urry, C. M., & Padovani, P. 1995, PASP, 107, 803

Weaver, J. R., Kau mann, O. B., Ilbert, O., et al. 2022, The Astrophysical Journal Supplement Series, 258, 11, aDS Bibcode: 2022ApJS..258...11W. https://ui.adsabs.harvard.edu/abs/2022ApJS..258...11W

Appendix

The photometric filters used to make all SEDs in this work are described in Table A.1. We use a total of 20 different filters spanning from the far-ultraviolet to the far-infrared.

Telescope/Instrument or Survey	Filter	Reference Wavelength [Å]
GALEX	FUV	1535.08
	NUV	2300.79
Subaru/HSC	g	4798.21
	r	6218.44
	i	7727.02
	z	8908.50
	y	9775.07
VISTA/VIRCAM	J	12524.83
	H	16432.40
	Ks	21521.52
Spitzer/SPLASH	Ch1	35378.41
	Ch2	44780.49
	Ch3	56961.77
	Ch4	77978.39
Spitzer/MIPS	24	235934.61
Herschel/Pacs	green	1.01e+6
	red	1.62e+6
Herschel/SPIRE	PSW	2.48e+6
	PMW	3.48e+6
	PLW	5.00e+6

Table A.1: Photometry from COSMOS2020 used to make SEDs. The left column shows the Telescope and instrument use to take get photometric measurements, the center column shows the name of the photometric lter, and the right column shows the reference wavelength in Angstroms.